ARTICLE

HLA-A$^+$ tertiary lymphoid structures with reactivated tumor infiltrating lymphocytes are associated with a positive immunotherapy response in esophageal squamous cell carcinoma

Dandan Zhang[1,2,9], Dongxian Jiang[3,9], Liping Jiang[4,9], Jiakang Ma[1,2,9], Xiaobing Wang[4], Xingyu Xu[1,2], Ziqiang Chen[1,2], Mengping Jiang[1,2], Wenjing Ye[5], Jie Wang[6], Weida Meng[1,2], Wenqing Qiu[7], Yingyong Hou[3], Jing Huang[8], Yuchen Jiao[4]✉, Yun Liu[1,2]✉ and Zhihua Liu[4]✉

BACKGROUND: Immune checkpoint blockade (ICB) therapy provides remarkable clinical benefits for multiple cancer types. However, the overall response rate to ICB therapy remains low in esophageal squamous cell carcinoma (ESCC). This study aimed to identify biomarkers of ICB therapy for ESCC and interrogate its potential clinical relevance.

METHODS: We investigated gene expression in 42 treatment-naïve ESCC tumor tissues and identified differentially expressed genes, tumor-infiltrating lymphocytes and immune-related genes signatures associated with differential immunotherapy responses. We systematically assessed the tumor microenvironment using the NanoString GeoMx digital spatial profiler, single-cell RNA-seq and multiplex immunohistochemistry in ESCC. Finally, we evaluated the associations between HLA-A-positive tertiary lymphoid structures (TLSs) and patients' responses to ICB in 60 ESCC patients.

RESULTS: Tumor infiltrating B lymphocytes and several immune-related gene signatures, such as the antigen presenting machinery (APM) signature, are significantly elevated in ICB treatment responders. Multiplex immunohistochemistry identified the presence of HLA-A$^+$ TLSs and showed that TLS-resident cells increasingly express HLA-A as TLSs mature. Most TLS-resident HLA-A$^+$ cells are tumor-infiltrating T (TIL-T) or tumor-infiltrating B (TIL-B) lymphocytes. Digital spatial profiling of spatially distinct TIL-T lymphocytes and single-cell RNA-seq data from 60 ESCC tumor tissues revealed that *CXCL13*-expressing exhausted TIL-Ts inside TLSs are reactivated with elevated expression of the APM signature as TLSs mature. Finally, we demonstrated that HLA-A$^+$ TLSs and their major cellular components, TIL-Ts and TIL-Bs, are associated with a clinical benefit from ICB treatment for ESCC.

CONCLUSIONS: HLA-A$^+$ TLSs are present in ESCC tumor tissues. TLS-resident TIL-Ts with elevated expression of the APM signature may be reactivated. HLA-A$^+$ TLSs and their major cellular components, TIL-Ts and TIL-Bs, may serve as biomarkers for ICB-treated ESCC patients.

British Journal of Cancer; https://doi.org/10.1038/s41416-024-02712-9

BACKGROUND

Esophageal cancer is one of the deadliest tumors worldwide. In China, esophageal squamous carcinoma (ESCC) accounts for 90% of esophageal cancers. The prognosis for ESCC is poor, with five-year survival rates of only 20–30% [1–3]. Recent advances have been made in the treatment of ESCC with the use of immune checkpoint blockade (ICB) therapy. The ability of tumor infiltrating lymphocytes (TILs) to eliminate cancer cells is greatly hampered by the high expression of exhaustion markers, such as *PDCD1* and *CTLA-4*. It is believed that exhausted TILs can be reactivated to generate a tumor-reactive response upon the use of ICB therapy [4]. Two clinical trials have shown that ICB treatment can indeed prolong the survival of ESCC patients in comparison with the results achieved with traditional chemotherapy [5, 6]. However, the overall response rate to ICB therapy remains below 30% [7]. Thus, it is important to identify biomarkers capable of predicting the clinical benefit of ICB therapy.

Tertiary lymphoid structures (TLSs) are defined as areas with organized aggregation of T and B lymphocytes based on

[1]MOE Key Laboratory of Metabolism and Molecular Medicine, Department of Biochemistry and Molecular Biology, School of Basic Medical Sciences and Shanghai Xuhui Central Hospital, Fudan University, Shanghai, China. [2]State Key Laboratory of Medical Neurobiology and MOE Frontiers Center for Brain Science, Institutes of Brain Science, Fudan University, Shanghai, China. [3]Department of Pathology, Zhongshan Hospital, Fudan University, Shanghai, China. [4]State Key Laboratory of Molecular Oncology, National Cancer Center, National Clinical Research Center for Cancer, Cancer Hospital, Chinese Academy of Medical Sciences and Peking Union Medical College, 100021 Beijing, China. [5]Division of Rheumatology and Immunology, Huashan Hospital, Fudan University, Shanghai, China. [6]Departments of Thoracic Surgery, Fudan University Shanghai Cancer Center, Shanghai, China. [7]Shanghai Xuhui Central Hospital, Shanghai, China. [8]Department of Medical Oncology, National Cancer Center/National Clinical Research Center for Cancer/Cancer Hospital, Chinese Academy of Medical Sciences and Peking Union Medical College, Beijing, China. [9]These authors contributed equally: Dandan Zhang, Dongxian Jiang, Liping Jiang, Jiakang Ma ✉email: jiaoyuchen@cicams.ac.cn; yliu39@fudan.edu.cn; liuzh@cicams.ac.cn

Received: 6 January 2024 Revised: 1 May 2024 Accepted: 2 May 2024
Published online: 18 May 2024

pathological characteristics [8, 9] that recapitulate the architecture of secondary lymphoid organs (SLOs). Increased evidence has shown that the presence of TLSs is correlated with patients' positive responses to ICB treatment for multiple tumor types [10], including melanoma [11, 12], soft tissue sarcoma [13], and renal cell carcinoma [11]. However, it is unclear whether TLSs can predict the clinical efficacy of ICB treatment in ESCC. Moreover, it is also unclear whether the microenvironment of TLSs has any effects on the reactivation of TILs, leading to an effective antitumor response to ICB treatment.

In the present work, we investigated gene expression in treatment-naïve ESCC tumor tissues and observed that several immune-related gene signatures, such as the antigen presenting machinery (APM) signature, are significantly elevated in ICB treatment responders before treatment. Multiplex immunohistochemistry (mIHC) identified the presence of HLA-A$^+$ TLSs and observed an increase in HLA-A expression by resident cells as TLSs mature, marked by the emergence of CD23$^+$ germinal centers (GCs). Most TLS-resident HLA-A$^+$ cells are tumor-infiltrating T (TIL-T) or tumor-infiltrating B (TIL-B) lymphocytes. Digital spatial profiling (DSP) of spatially distinct TIL-T lymphocytes and large single-cell RNA-seq (scRNA-seq) data from 60 ESCC tumor tissues revealed that *CXCL13*-expressing exhausted TIL-Ts inside TLSs are reactivated with elevated expression of the APM signature as TLSs mature. Finally, we demonstrated that HLA-A$^+$ TLSs and their major cellular components, TIL-Ts and TIL-Bs, are associated with a clinical benefit from ICB treatment for ESCC.

METHODS

Cohorts and sample collection

Cohort 1 includes a group of ESCC patients ($n = 42$) who received anti-PD-1 blockade at the Cancer Hospital of the Chinese Academy of Medical Science in Beijing, China. Surgically resected or biopsied tumor tissues were collected as formalin-fixed paraffin-embedded (FFPE) tissues before ICB treatment. The clinical response for each patient was evaluated after ICB treatment based on RECIST [14] (Fig. 1a). Responders were defined as patients diagnosed with a complete response or partial response; and non-responders were defined as patients diagnosed with stable disease or progressive disease.

Cohort 2 includes a group of ESCC patients ($n = 60$) who received neoadjuvant therapy combined with anti-PD-1 and chemotherapy at Zhongshan Hospital of Fudan University in Shanghai, China. Tumor tissues were surgically resected as FFPE tissues after one to four cycles of treatment. The clinical response for each individual was evaluated before the surgery based on RECIST. Responders were defined as patients with a complete response or partial response; and non-responders were defined as patients diagnosed with stable disease or progressive disease.

The clinical characteristics of both cohorts are summarized in Supplementary Table S1.

RNA-seq

RNA was extracted from the FFPE tumor tissues of cohort 1 using a QIAgen RNeasy FFPE kit according to the manufacturer's instructions. The RNA-seq libraries were constructed using an Illumina TruSeq RNA Exome Library Preparation Kit. All libraries were sequenced on an Illumina Hiseq X Ten sequencer with the paired-end mode of 2 ×150 bp.

Analysis of RNA-seq data

Gene expression in each sample was evaluated by pseudoalignment of the trimmed RNA-seq reads to the human transcriptome (gencode V43, GRCh38) using Kallisto (v0.46.1) [15]. The quality of each sample was evaluated to only include samples in which the coverages of protein-coding genes exceeded 70%. A total of seventeen samples were excluded based on this criterion (Supplementary Table S1), likely due to a high degree of RNA degradation in FFPE tissues. The counts of protein-coding genes were processed by the DESeq2 package (v1.28.1) to identify DEGs (differential expressed genes) between the responder and non-responder groups. A cut-off of gene expression fold change >2 or <0.5 and an FDR < 0.05 was used to identify DEGs.

Estimation of tumor-infiltrating immune cells

The online software CIBERSORT (https://cibersort.stanford.edu) was used on the normalized expression data to estimate the proportions of six major tumor-infiltrating immune cells (B cells, CD4$^+$ T cells, CD8$^+$ T cells, NK cells, monocytes, and neutrophils). The statistical differences between the responder and non-responder groups were calculated using a two-sided Wilcoxon rank sum test.

Gene set enrichment analysis (GSEA)

GSEA was performed on the RNA-seq data with clusterProfiler v4.2.2 [16], and both biological databases (GO and KEGG) were evaluated with a significant cut-off of adjusted P value < 0.05.

B cell receptor analysis

The BCR assembly algorithm MiXCR v3.0.13 [17] was utilized to extract the B cell immunoglobin hypervariable regions from the bulk RNA-seq data to assemble the complementarity determining region 3 (CDR3) sequences of IgH and IgK and IgL. The MiXCR output was parsed with the R package immunarch v0.6.5 for downstream analysis. B cell entropy was calculated using immunarch for the assessment of BCR diversity. Normalized B cell entropy was calculated by division of log2 of the number of unique productive CDR3 sequences to adjust the total number of reads in each sample. B cell clonality is defined as the reciprocal of normalized B cell entropy (clonality = 1 − normalized entropy) with values ranging from 0 (most diverse) to 1 (least diverse) [18].

The Cancer Genome Atlas (TCGA) data analysis

RNA-seq and clinical data for esophageal cancer (ESCA) patients from the TCGA were downloaded from UCSC Xena (http://xena.ucsc.edu/). Only squamous cell carcinoma (ESCC, $n = 82$) cases were included for the analysis. We calculated the expression level of the APM signature with log2-normalized expression profiles, and the Pearson correlation coefficient was calculated between the expression of *HLA-A* and the APM signature.

Multiplex immunohistochemistry (mIHC)

Multiplex immunohistochemistry staining was performed on 4-μm section slides of FFPE tumor tissues of four patients from cohort 1 and 60 patients from cohort 2. Mouse or rabbit anti-human monoclonal antibodies were used for staining as follows: HLA-A (A11406, Abclonal), CD20 (14-0202-82, eBioscience), and CD3 (ab16669, Abcam). The stained slides were blocked with fluorescence mounting medium and visualized with the Vectra Polaris image system (Perkin Elmer).

Immunohistochemistry staining of CD23

Immunohistochemistry staining of CD23 was performed on section slides of FFPE tumor tissues of 60 patients from cohort 2. The slides were stained with a primary antibody against CD23 (M-0104, Long Island) and visualized with the Vectra Polaris image system (Perkin Elmer). Mature TLSs were defined by the presence of a network of CD23$^+$ cells based on immunohistochemistry staining of identified TLSs.

mIHC data analysis and TLS segmentation

mIHC-stained slides from 60 patients in cohort 2 were scanned for multispectral image acquisition using the Vectra Polaris image system (Perkin Elmer) with the following channels: Opal 570 for HLA-A, Opal 520 for CD3, and Opal 690 for CD20. The scanned slides were visualized with Phenochart (Perkin Elmer). All regions with the size of 930 μm × 697 μm containing aggregated lymphocytes on the slides were manually selected based on CD20 and CD3 staining, and the segmentation and quantification protocols for the TLS areas were conducted using inForm image analysis software (Perkin Elmer). Briefly, inForm was first used for cell segmentation, and the positive threshold of each marker was determined and recorded for further data analysis. Representative images of regions containing aggregated lymphocytes were selected, and the TLS areas were manually segmented based on CD3 and CD20 staining. Manually segregated representative images were then used to establish a TLS segmentation algorithm so that the TLS areas contained at least 50 CD3$^+$ or CD20$^+$ lymphocytes. Once the algorithm was complete, all images were imported into inForm and run as a batch to segment into the TLS and non-TLS areas.

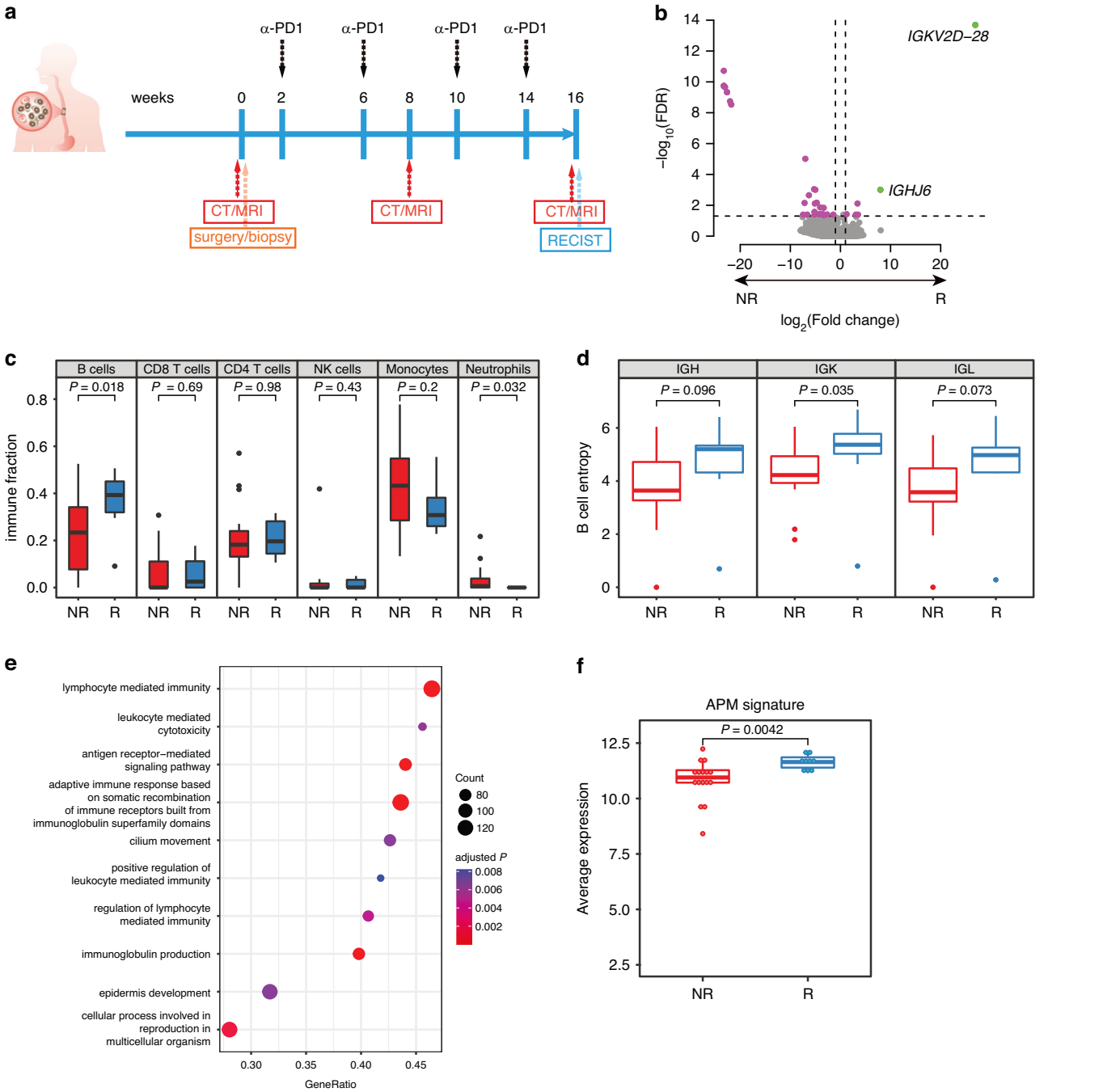

Fig. 1 Tumor-infiltrating B (TIL-B) lymphocytes and the APM expression are elevated in ICB-responsive ESCC patients. a Timeline for cohort 1. The anti-PD1 treatment was started two weeks post- surgery and administered at four-week intervals. The clinical response for each patient was assessed in accordance with RECIST criteria, using CT or MRI data performed before the surgery, and subsequently at weeks 8 and 16. **b** Volcano plot showing 36 differentially expressed genes (indicated by purple points) identified by RNA-seq of treatment-naïve ESCC tumor tissues biopsied from responders (R, $n = 9$) and non-responders (NR, $n = 16$). A cutoff of gene expression fold change >2 or <0.5 and false discovery rate (FDR) < 0.05 was used. Two differentially expressed immunoglobulin genes are highlighted in green. **c** Boxplot showing the estimation of tumor-infiltrating immune cells using CIBERSORT [25, 26]. The *P* values were calculated using a two-sided Wilcoxon rank-sum test comparing responders (R) with non-responders (NR). **d** B cell entropy of each individual were estimated from the RNA-seq data using MiXCR. Both the immunoglobulin heavy (IgH) and light (IgK and IgL) chain molecules in the R and the NR groups are shown. **e** Top 10 significant gene sets identified by GSEA with adjusted *P* values < 0.05. **f** Responders' tumors featured significantly elevated expression of an antigen presenting machinery (APM) signature. The *P* value indicated at the top was calculated using a two-sided Wilcoxon rank sum test. In **c**, **d** and **f**: Middle line, median; box edges, 25th and 75th percentiles; whiskers, most extreme points that do not exceed ±interquartile range (IQR) ×1.5; further outliers are marked individually.

HLA-A$^+$ TLS quantification

Expert pathologists segmented the tumor bed manually in the resected primary tumors from cohort 2. We only evaluated the TLSs in the tumor bed. HLA-A$^+$ TLSs were defined as TLSs in which the percentage of HLA-A$^+$ cells exceeded the first quantile of HLA-A$^+$ cells among all TLS-resident cells (65%). Only TLSs with an area larger than 60,000 μm^2, comprising at

least 700 cells and 350 B lymphocytes, were included in the statistical analyses [13]. The normalized number and area of HLA-A$^+$ TLSs for each individual was calculated by dividing the number and area of HLA-A$^+$ TLSs by the area of the tumor bed (per mm^2) in each slide.

NanoString GeoMx DSP

One patient from cohort 2 was selected for the evaluation with NanoString GeoMx DSP. Tissue morphology was visualized using antibodies against CD3 (UM500048CF, Origene), CD19 (ZM-0038, Beijing Zhong Shan-Golden Bridge), and HLA-A (A11406, Abclonal). Human Whole Transcriptome Atlas (WTA) probes targeting over 19,000 targets were hybridized, and the slide was loaded on a NanoString GeoMx digital spatial profiler (DSP). Three sets of AOIs (areas of interest) were selected to include HLA-A$^-$CD19$^-$CD3$^+$ TIL-Ts outside TLSs ($n = 5$), HLA-A$^-$CD19$^-$CD3$^+$ TIL-Ts inside TLSs ($n = 2$), and HLA-A$^+$CD19$^-$CD3$^+$ TIL-Ts inside TLSs ($n = 4$). The GeoMx DSP exposed each AOI to ultraviolet light to release and collect the UMI-containing oligos from the WTA probes. Sequencing libraries were constructed subsequently according to the manufacturer's instructions.

NanoString GeoMx DSP analysis

The DSP data from 11 AOIs were first preprocessed by the NanoString GeoMx DSP NGS pipeline and then converted to the gene expression matrix of digital count conversion (DCC) files according to the manufacturer's instructions. The quality of each AOI was evaluated using the R package GeomxTools, with one AOI (HLA-A$^+$CD19$^-$CD3$^+$ TIL-Ts inside TLSs) removed because of an extremely high number of negative probes. The limit of quantitation (LOQ) per AOI was defined as the geometric mean of the negative probes × geometric standard deviation of negative probes squared. Genes with an expression level below LOQ in each AOI were excluded from further analysis. The remaining 5887 genes in 10 AOIs were utilized to identify differentially expressed genes using DESeq2 package v1.28.1 [19].

scRNA-seq preprocessing

Raw scRNA-seq data from CD45 immune cells sorted from 60 ESCC patients were obtained from Gene Expression Omnibus under accession code GSE160269. Cell Ranger v7.0.0 provided by 10× Genomics was used for cellular barcode demultiplexing, read mapping, and gene count generation. We used Seurat v4.1.1 [20] to generate the gene expression matrix for each individual. For quality control, we excluded genes expressed in fewer than three cells. We further excluded cells with unique feature counts under 500 or over 2000–6000 based on the feature count density per sample. We also excluded cells with over 10% mitochondrial reads or UMI counts below 1000. The DoubletFinder v2.0.3 [21] was used to remove potential cell doublets. After quality control, the Seurat objects of all individuals were merged and normalized to generate the expression matrix using the LogNormalize method.

scRNA-seq clustering

We selected the 2000 most variable features using the vst method in Seurat for data scaling and subsequent clustering. Harmony v1.0 [22] was used to correct patient-specific batches. The batch-corrected Seurat object was subjected to dimension reduction using uniform manifold approximation and projection (UMAP). The shared nearest neighbor (SNN) graph was constructed using the FindNeighbors command based on the first 50 Harmony components, and Louvian clustering was conducted using the FindClusters command with a resolution parameter of 0.8.

Identification of cell types

The singleR v1.8.1 [23] with HumanPrimaryCellAtlasData dataset was first used to identify potential cell types. Next, the cell type annotation was manually curated. Specifically, the FindAllMarkers command with Wilcoxon rank sum test from the Seurat package was used to identify differentially expressed genes for each cluster, and the cell type annotation for each cluster was confirmed by elevated expression of known marker genes (T cells: *CD3D*, *CD3E*, *CD3G*, and *CD2*; B cells: *CD19*, *CD79A*, *MS4A1*, *JCHAIN*, and *MZB1*; myeloid cells: *CD68*, *LYZ*, *CD14*, and *IL3RA*; and common myeloid progenitor cells (CMPs): *TPSAB1*) (Supplementary Fig. S1a, b).

Analysis of the CD8$^+$ T cell population

Clusters of CD4 and CD8 T cells were identified by the expression of CD4 or CD8 (Supplementary Fig. S1c, d). We conducted a series of analyses on the CD8$^+$ T cells to identify exhausted CD8$^+$ T (Tex) cells. We first identified and extracted CD8$^+$ T cells with high expression of three exhaustion markers (*PDCD1*, *TIGIT*, and *CTLA4*) for further analysis (Supplementary Fig. S1e, f). Among these CD8$^+$ T cells expressing exhaustion markers, a subset was identified and excluded based on the expression of proliferation-associated genes *TUBB*, *STMN1*, and *MKI67* (Supplementary Fig. S1g, h). We further excluded CD8$^+$ T cells with specific TCR sequences (Supplementary Fig. S1g), leaving 8689 Tex cells for the downstream analyses.

Monocle2 v2.22.0 [24] was used for the pseudotime analysis of these Tex cells. We selected the 2028 most variable genes for cell ordering. Dimension reduction and cell trajectory construction were performed on these selected genes with default settings. Based on the pseudotime pattern of all the cells, the clusters of Tex identified by Seurat were reclassified into four states along the linear trajectory (defined as Tex_S1 through Tex_S4). The differentially expressed gene analysis was performed on Tex_S3 and Tex_S4, the last two Tex cell states along the pseudotime trajectory. GSEA based on GO was conducted using clusterProfiler v4.2.2 [16].

Analysis of the CD4$^+$ T cell population

We conducted similar analyses on CD4$^+$ T cells to identify and extract $CD4_{CXCL13}$ cells. Among the CD4$^+$ T cells, those with high expression of *PDCD1*, *TIGIT*, and *CTLA4* were first identified and extracted (Supplementary Fig. S2a, b). Among these CD4$^+$ T cells expressing exhaustion markers, a subset was identified and excluded based on the expression of *FOXP3*, a lineage marker of regulatory T cells (Supplementary Fig. S2c). The remaining cells expressing *CXCL13* ($CD4_{CXCL13}$) (Supplementary Fig. S2d) were extracted and used for the downstream analyses.

Monocle2 v2.22.0 was used for the pseudotime analysis of $CD4_{CXCL13}$ cells. The 1818 most variable genes were selected for cell ordering. Dimension reduction and cell trajectory construction were conducted on these genes using default settings. Based on the pseudotime pattern of all these cells, we reclassified cell clusters identified by Seurat into four different states (defined as $CD4_{CXCL13}$_S1 through $CD4_{CXCL13}$_S4). Differentially expressed genes between $CD4_{CXCL13}$_S3 and $CD4_{CXCL13}$_S4, the last two $CD4_{CXCL13}$ cell states along the pseudotime trajectory, were identified with the FindMarkers function. GSEA based on GO was conducted using clusterProfiler v4.2.2 [16].

Analysis of the B cell population

Extracted B cells were further clustered to identify subpopulations. Briefly, the 2000 most variable genes were identified from the B cell expression data and used for clustering. The SNN graph was constructed with the first 20 components using the FindNeighbors command. Subsequently, Louvian clustering was performed using the FindClusters command with a resolution parameter of 0.2. B cell subpopulations were manually annotated based on the following marker genes: Naïve B: *FCER2* and *IGHD*; Plasma B: *IGHG1*, *IGLV2-14*, *IGKC*, *JCHAIN*, *MZB1*, and *XBP1*; GC B: *RGS13*, *TCL1A*, *BACH2*, and *NEIL1*; Follicular B: *TNFRSF13B*, *CD70*, *BANK1*, and *HLA-A*; and Memory B: *FCRL4*, *CD86*, and *ISG15* (Supplementary Fig. S3a, b).

Statistical analysis

All statistical analyses were performed using R language (version 4.1.2). The associations between two quantitative variables were estimated with the Pearson correlation. Group comparisons were evaluated using two-sided Wilcoxon rank sum test or two-sided Student's *t* test (data followed normal distribution and variance is similar between the two groups based on the F-test), as specified in the methods or figure legends. *P* values were corrected for multiple hypothesis testing using the Benjamini-Hocheberg method where appropriate.

RESULTS

Tumors of ICB-responsive ESCC patients feature elevated expression of an antigen presenting machinery signature

Our initial investigation of differential immunotherapy responses was based on a set of treatment-naïve tumor tissues from ESCC patients (cohort 1) ($n = 42$, Supplementary Table S1) who each received anti-PD-1 blockade and had their clinical responses evaluated based on the Response Evaluation Criteria in Solid Tumors (RECIST) v1.1 [14] (Fig. 1a). We conducted an RNA-seq analysis of these ESCC tumor tissues. After excluding seventeen

samples that failed quality control, we detected 35 differentially expressed genes between 9 responders and 16 non-responders (Supplementary Table S2). The expression of two immunoglobulin genes (*IGKV2D-28* and *IGHJ6*) was significantly elevated in the responders (Fig. 1b and Supplementary Fig. S4a). Since immunoglobulin genes are exclusively expressed in the B cell lineage, we estimated immune cell infiltration in each sample based on the RNA-seq data [25, 26]. The responders had significantly more TIL-B lymphocytes than the non-responders ($P = 0.018$, two-sided Wilcoxon rank sum test) (Fig. 1c). We subsequently assembled B cell receptor (BCR) sequences from the RNA-seq data and observed significantly higher B cell entropy for the immunoglobulin light chain molecule (IgK) in ICB-responsive patients (Fig. 1d). However, after adjusting the number of unique productive CDR3 sequences in each sample, no differences were observed in BCR clonalities, which reflect the presence of B cell clonal expansion [27] (Supplementary Fig. S4b). This finding suggests that an elevated level of TIL-B lymphocytes without clonal expansion in treatment-naïve ESCC tumor tissues may promote the efficiency of ICB treatment.

Gene set enrichment analysis (GSEA) of the RNA-seq data revealed that the responders' tumors featured elevated expression of several immune-related gene sets (Fig. 1e). An evaluation of previously defined gene signatures capable of predicting immunotherapy response in other tumor types revealed that ESCC tumors in the responder group featured significantly elevated expression of gene signatures of IFN-γ [28] ($P = 0.014$) (Supplementary Fig. S4c) and antigen presenting machinery (APM) [29] ($P = 0.0042$) (Fig. 1f). We individually examined the expression levels of all seven genes in the APM signature and found that three genes, including *HLA-A*, *HLA-B* and *TAPBP*, demonstrated significantly elevated expression levels in the responders ($P < 0.05$) (Supplementary Fig. S4d). Thus, the elevated expression of immune-related gene signatures, including the APM signature, can potentially account for the differential responsivity to ICB treatment in ESCC. Moreover, the high correlations among these features (Supplementary Fig. S5), including the APM expression and the abundance of TIL-Bs, suggest that they may be mechanistically related in determining ESCC patients' responses to ICB treatment.

The presence of HLA-A$^+$ tertiary lymphoid structures

We performed mIHC staining on four treatment-naïve ESCC tumor tissues from cohort 1 to identify cells expressing the APM signature and their interactions with TILs, mainly TIL-Ts and TIL-Bs. Because of the strong correlations between the expression levels of *HLA-A* and the APM signature observed in our data and among ESCC patients from the Cancer Genome Atlas (TCGA) (Supplementary Fig. S6), we stained for the HLA-A protein as a surrogate measurement of the APM signature. We found that CD3$^+$ TIL-T and CD20$^+$ TIL-B lymphocytes often aggregate densely (Fig. 2a, b) and form structures referred to as TLSs [9]. There were 43 regions identified with aggregated TILs, which we divided into TLS and non-TLS areas (Supplementary Fig. S7). The TLS areas had significantly higher percentages of HLA-A$^+$ cells than the non-TLS areas (Fig. 2c). We interrogated the colocalization of the HLA-A signal with CD20 or CD3 staining and found that over 60% of TLS-resident HLA-A$^+$ cells were CD20$^+$ TIL-B or CD3$^+$ TIL-T lymphocytes (Fig. 2d).

We analyzed another set of ESCC tumor tissues surgically resected after one to four cycles of neoadjuvant therapy with combined anti-PD-1 and chemotherapy (cohort 2) ($n = 60$, 36 responders vs. 24 non-responders, Supplementary Table S1) to investigate whether ICB treatment affects HLA-A$^+$ TLSs. mIHC staining of all these resected tissues (Supplementary Fig. S8a) showed that over 76% of HLA-A$^+$ cells reside in the TLS areas (Supplementary Fig. S8b), and over 82% of TLS-resident HLA-A$^+$ cells are CD20$^+$ TIL-B or CD3$^+$ TIL-T lymphocytes (Supplementary Fig. S8c), similar to our observations with treatment-naïve ESCC tumor tissues. These findings demonstrate that HLA-A$^+$ TLSs are present in ESCC tumor tissues before and after ICB treatment, and most TLS-resident HLA-A$^+$ cells are TIL-T or TIL-B lymphocytes.

TLS-resident TIL-Ts express HLA-A as TLSs mature

Similar to SLOs, mature intra-tumoral TLSs can be characterized by compartmentalized B cell zones known as GCs expressing CD23 [8]. We performed additional immunohistochemistry staining of CD23 on the consecutive slides stained previously for CD3, CD20, and HLA-A from cohort 2 to investigate HLA-A expression in TLS-resident TILs as TLSs mature. Among the 679 TLSs identified, the CD23$^+$ mature TLSs (Supplementary Fig. S9a) exhibited significantly higher percentages of HLA-A$^+$ cells compared to the CD23$^-$ immature TLSs (Supplementary Fig. S9b, c) (Fig. 3a). This result suggests that TLS-resident cells increasingly express HLA-A as TLSs mature.

We performed NanoString GeoMx DSP on spatially distinct TIL-Ts to identify differentially expressed genes through the maturation of TLSs. Two sets of areas of interest (AOIs) inside TLSs were selected to collect HLA-A$^-$ or HLA-A$^+$ CD19$^-$CD3$^+$ TIL-Ts based on CD3, CD19, and HLA-A staining (Fig. 3b). Another set of AOIs outside TLSs was selected to collect HLA-A$^-$CD19$^-$CD3$^+$ TIL-Ts (Fig. 3b). Consistent with the mIHC staining, the expression of *HLA-A* was significantly higher in HLA-A$^+$ TIL-Ts inside TLSs than in HLA-A$^-$ TIL-Ts inside and outside TLSs ($P = 0.033$) (Supplementary Fig. S10a).

It has been reported that a majority of TIL-Ts are in a exhausted state, with elevated expression of immune checkpoint genes [30]. Consistent with this, we observed sustained expression of exhaustion markers, including *PDCD1* (Supplementary Fig. S10b), *TIGIT* (Supplementary Fig. S10c), and *CTLA4* (Supplementary Fig. S10d), in TIL-Ts from all three sets of AOIs, indicating that they mainly include exhausted TIL-Ts regardless of their location. Differentially expressed gene analysis under a linear regression model of three sets of AOIs revealed that the expression of a chemokine, *CXCL13*, was significantly elevated in TLS-resident HLA-A$^+$ TIL-Ts (adjusted $P = 0.0044$) (Fig. 3c). This is consistent with recent findings that *CXCL13*-expressing TIL-Ts recruit lymphocytes to form and maintain TLSs in breast cancer [31, 32], lung cancer [33, 34], and bladder cancer [35]. Interestingly, GSEA revealed that TLS-resident HLA-A$^+$ TIL-Ts featured significantly elevated expression of multiple gene sets related to T cell activation (Fig. 3d, e). These results indicate that, even though *CXCL13*-expressing TIL-Ts inside TLSs are exhausted with sustained expression of exhaustion markers, they may be reactivated with the APM expression as TLSs mature.

Exhausted TIL-Ts with elevated expression of the APM signature are reactivated

We leveraged a large scRNA-seq dataset from 60 treatment-naïve ESCC tumor tissues [36] to investigate the aforementioned gene expression changes at the single-cell level. We identified and extracted 24,926 B cells, 52,484 CD8$^+$ T cells, and 39,393 CD4$^+$ T cells from a total of 151,058 high-quality CD45$^+$ immune cells (Supplementary Fig. S1a–d). Among them, 8,689 exhausted CD8$^+$ T (Tex) cells (Supplementary Fig. S1e–h) and 13,496 exhausted CD4$^+$ T cells (Supplementary Fig. S2a, b) were identified based on their high expression of exhaustion markers, including *PDCD1*, *TIGIT*, and *CTLA4*. Exhausted CD4$^+$ T cells can be further divided into two clusters based on the expression of *FOXP3*, a lineage marker of regulatory T cells (Supplementary Fig. S2c). The cells in the cluster without the expression of *FOXP3* appeared to express *CXCL13* ($CD4_{CXCL13}$) (Supplementary Fig. S2d). Thus, we focused on these identified Tex and $CD4_{CXCL13}$ cells in the downstream analyses.

We performed the single-cell trajectory analysis of Tex cells and observed a single lineage with four different states based on the pseudotime expression pattern (Fig. 4a). State 1 of Tex (Tex_S1) cells

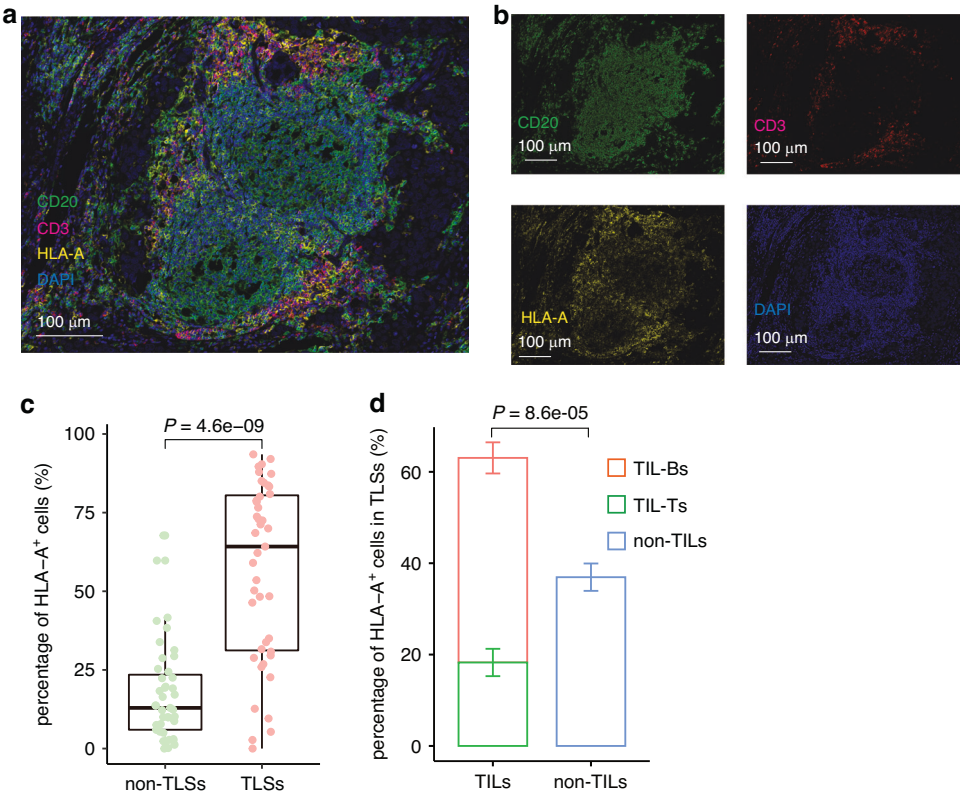

Fig. 2 The presence of HLA-A$^+$ TLSs in treatment-naïve ESCC tumors. a Multiplex immunohistochemistry (mIHC) staining of CD20, CD3, and HLA-A, together with DAPI, in a representative image of an HLA-A$^+$ TLS. **b** Separate images showing the four single-color channels from A. **c** Each region with aggregated TILs was further divided into TLS and non-TLS areas. The percentage of HLA-A$^+$ cells in each area was calculated by dividing the number of HLA-A$^+$ cells by the total number of cells in that area. Middle line, median; box edges, 25th and 75th percentiles; whiskers, most extreme points that do not exceed ± interquartile range (IQR) ×1.5; further outliers are marked individually. The *P* value indicated at the top was calculated using a Wilcoxon rank-sum test. **d** Stacked bar plot showing the percentages of HLA-A$^+$ TILs (including both TIL-Ts in green and TIL-Bs in red) or other cell types (non-TILs in blue) in TLSs. Data are represented as the mean ± SEM. The *P* value indicated at the top was calculated using a two-sided paired Student's *t* test.

appeared to represent progenitor Tex with elevated expression of *TCF7*, *IL7R*, and *CCR7* (Fig. 4b). Tex_S1 cells are analogous to the stem-like subset of PD-1$^+$Tcf1$^+$CD8$^+$ T cells [37–39] with elevated expression of *EOMES, TCF7* and *CD28* (Supplementary Fig. S11a). The stem-like progenitor Tex has the potential to proliferate and differentiate into terminal Tex [37, 38, 40] and are linked to positive outcomes in ICB-treated melanoma [41, 42] and several mouse models [41, 43, 44]. Tex cells from state 2 to state 4 are distinct from progenitor stem-like Tex (Tex_S1) with elevated expression of *HAVCR2* (*Tim3*) and *ENTPD1* (*CD39*) (Supplementary Fig. S11b), which are similar to previously reported Tim3$^+$PD1$^+$ terminal Tex [37–39, 45]. An investigation of *CXCL13*, which is involved in the transition from progenitor Tex to terminal Tex [34], revealed that its expression started to increase in state 3 (Tex_S3) and continued to increase in state 4 (Tex_S4) (Fig. 4c), consistent with our DSP observations (Fig. 3c). An investigation of the APM expression showed that the expression of this signature, along with the majority of genes within it, also started to increase in Tex_S3 and continued to increase in Tex_S4 (Fig. 4d, Supplementary Fig. S12a), suggesting that *CXCL13*-expressing TIL-Ts in TLSs begin to express the APM signature as TLSs mature.

We performed a differentially expressed gene analysis to identify the determinants responsible for Tex cells switching from Tex_S3 to Tex_S4 and found that the expression of *HLA-DRA* and the co-stimulatory receptor *TNFRSF9* (*4-1BB*) was significantly higher in Tex_S4 than in Tex_S3 (Fig. 4e). Moreover, the expression levels of cytotoxic immunity-related genes *IFNG*, *GZMB*, and *GNLY* were also significantly increased in Tex_S4 (Fig. 4e), indicating the potential reactivation of tumor-reactive Tex cells [46–48]. GSEA revealed that Tex_S4 cells featured significantly elevated expression of multiple gene sets related to T cell activation (Fig. 4f), similar to our DSP observations (Fig. 3d, e). These results indicate that exhausted Tex_S4 cells, characterized by elevated expression of the APM signature, could potentially be reactivated to bolster CD8$^+$ T cell-mediated cytotoxicity in antitumor response, which aligns with previous findings that *CXCL13*-expression exhausted CD8$^+$ T cells serve as a positive indicator for non-small-cell lung cancer patients undergoing ICB therapy [33, 34].

Trajectory analysis of $CD4_{CXCL13}$ cells revealed a similar pseudotime expression lineage of four different states (Fig. 4g). Similar to Tex cells, state 1 of $CD4_{CXCL13}$ ($CD4_{CXCL13}$_S1) cells represents progenitor cells with highly expressed *TCF7*, *IL7R*, and *CCR7* (Fig. 4h). The expression of *CXCL13*, the APM signature, and the majority of genes within it begin to increase in state 3 ($CD4_{CXCL13}$_S3) and continue to increase in state 4 ($CD4_{CXCL13}$_S4) (Fig. 4i, j, Supplementary Fig. S12b). Moreover, the expression of cytokine, *IFNG* (Fig. 4k), and the co-stimulatory receptors, *TNFRSF9* (*4-1BB*) and *TNFSF14* (Supplementary Fig. S11c), is significantly elevated in $CD4_{CXCL13}$_S4. Similar to Tex cells, the differentially expressed gene analysis between $CD4_{CXCL13}$_S3 and $CD4_{CXCL13}$_S4 revealed that the expression levels of multiple gene sets related to T cell activation are significantly enriched in $CD4_{CXCL13}$_S4 (Fig. 4l). The expression of ligand-receptor pairs between $CD4_{CXCL13}$ and five subtypes of B cells (Supplementary Fig. S3a, b) revealed that $CD4_{CXCL13}$_S4 cells may exert helper-like functions on the proliferation, differentiation, and

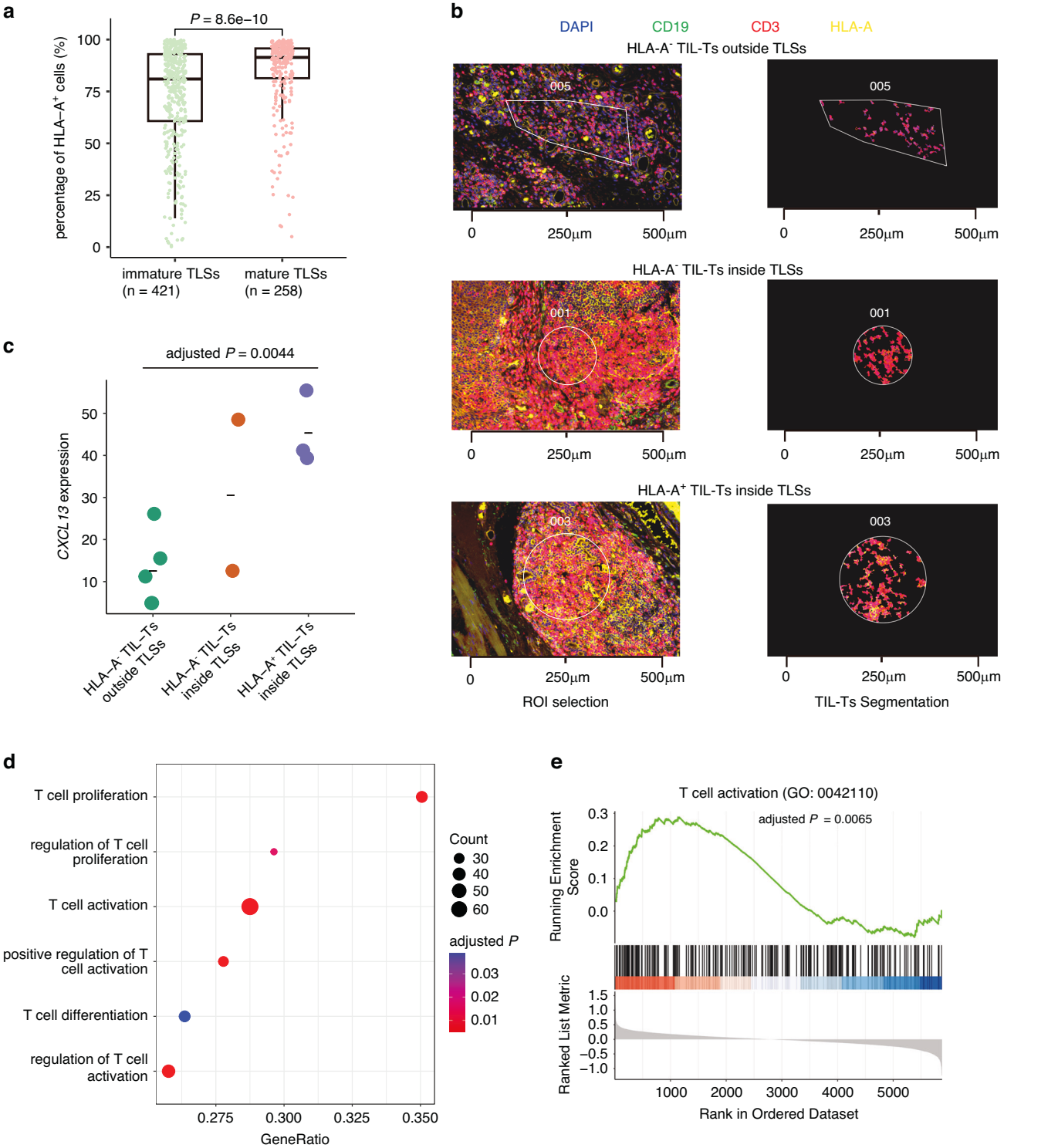

Fig. 3 TLS-resident TIL-Ts begin expressing the APM signature as TLSs mature. a Percentages of HLA-A$^+$ cells within TLSs in mature TLSs and immature TLSs, with the *P* value (two-sided Wilcoxon rank-sum test) indicated at the top. **b** Representative images showing the selection of AOIs with mIHC staining of CD3, CD19, and HLA-A. Three sets of spatially distinct CD19$^-$CD3$^+$ TIL-Ts were collected for DSP: 1. HLA-A$^-$ TIL-Ts outside TLSs (the top row, $n = 5$); 2. HLA-A$^-$ TIL-Ts inside TLSs (the middle row, $n = 2$); and 3. HLA-A$^+$ TIL-Ts inside TLSs (the bottom row, $n = 4$). **c** Expression of *CXCL13* is significantly elevated in TLS-resident HLA-A$^+$ TIL-Ts under a linear regression model on three sets of AOIs, with the adjusted *P* value indicated at the top. Middle line, mean. **d** Six significant Gene Ontology (GO) gene sets identified by GSEA, with adjusted *P* values < 0.05. **e** TLS-resident HLA-A$^+$ TIL-Ts featured significantly elevated expression of a T cell activation gene set (GO: 0042110).

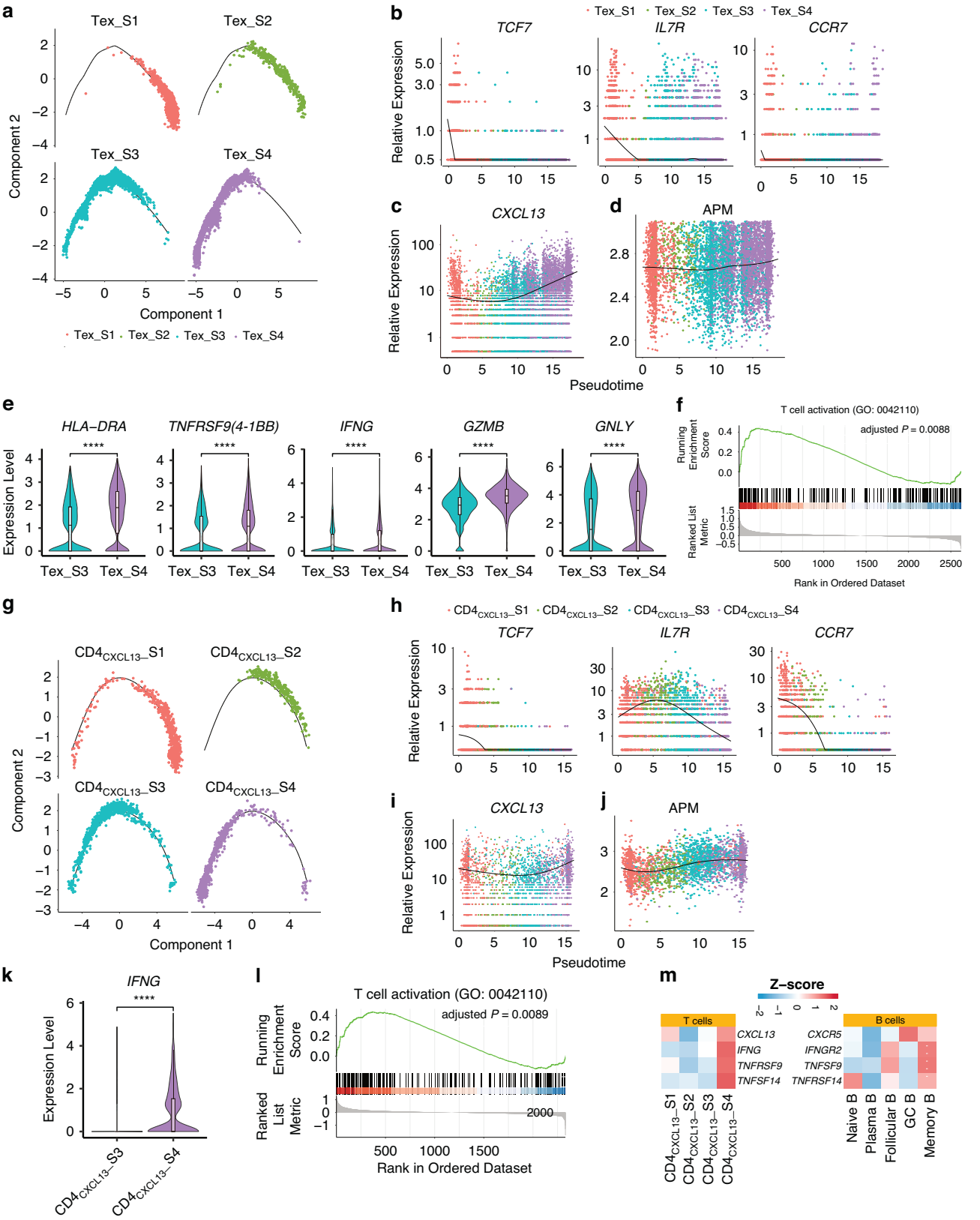

maturation of B cells through the expression of these cytokine and co-stimulatory receptors (Fig. 4m) [49–52].

Thus, throughout the process of TLS maturation, TLS-resident *CXCL13*-expressing exhausted TIL-Ts may be reactivated with elevated expression of the APM signature. Exhausted $CD8^+$ T cells may be reactivated for cytotoxic immunity, while exhausted $CD4^+$ T cells may be reactivated for humoral immunity through the regulation of TIL-B differentiation.

Fig. 4 Exhausted TIL-Ts with elevated expression of the APM signature are reactivated. a Pseudotime trajectory of Tex cells differentiating Tex_S1 through Tex_S4. **b** Pseudotime expression patterns of selected genes from Tex_S1 through Tex_S4. Pseudotime expression patterns of *CXCL13* (**c**) and the APM signature (**d**) from Tex_S1 through Tex_S4. **e** Expression of selected genes is significantly higher in Tex_S4 than in Tex_S3 (****$P < 0.0001$, Wilcoxon rank-sum test, two-sided). **f** Tex_S4 cells featured significantly elevated expression of a T cell activation gene set (GO: 0042110). **g** Pseudotime trajectory of $CD4_{CXCL13}$ cells differentiating $CD4_{CXCL13}$_S1 through $CD4_{CXCL13}$_S4. **h** Pseudotime expression patterns of selected genes from $CD4_{CXCL13}$_S1 through $CD4_{CXCL13}$_S4. Pseudotime expression patterns of *CXCL13* (**i**) and the APM signature (**j**) from $CD4_{CXCL13}$_S3 to $CD4_{CXCL13}$_S4. **k** Expression of *IFNG* is significantly higher in $CD4_{CXCL13}$_S4 than in $CD4_{CXCL13}$_S3 (****$P < 0.0001$, Wilcoxon rank-sum test, two-sided). **l** $CD4_{CXCL13}$_S4 cells featured significantly elevated expression of a T cell activation gene set (GO: 0042110). **m** Heatmap showing the expression of ligand-receptor pairs between B cell subtypes and four states of $CD4_{CXCL13}$ cells. In **e** and **k**: Middle line, median; box edges, 25th and 75th percentiles; whiskers, most extreme points that do not exceed ± interquartile range (IQR) ×1.5.

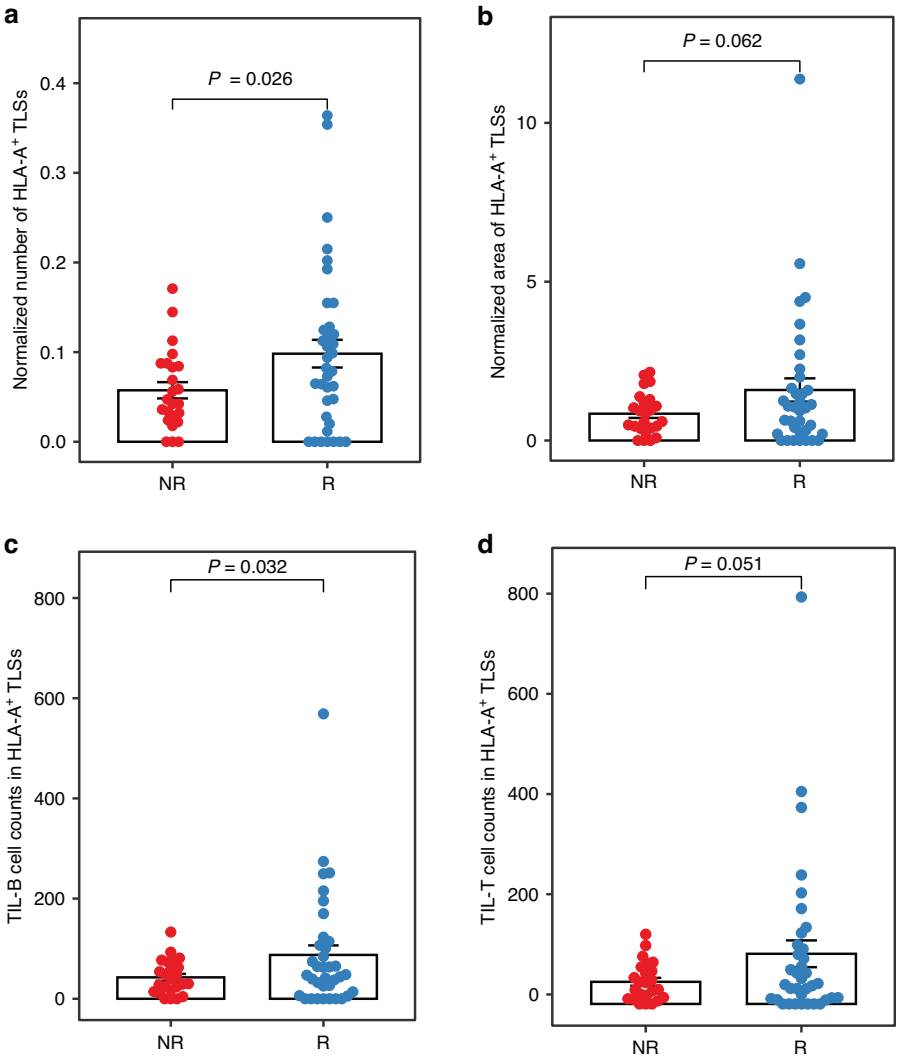

Fig. 5 HLA-A^+ TLSs are associated with a clinical benefit from ICB treatment for ESCC. a, **b** Quantification of HLA-A^+ TLSs was based on mIHC staining of CD3, CD20, and HLA-A. HLA-A^+ TLSs were defined as TLSs in which the percentage of HLA-A^+ cells is over 65%. The y-axis represents the number (**a**) or the area (μm^2) (**b**) of HLA-A^+ TLSs normalized by the area of the tumor bed (per mm^2). Data are represented as the mean ± SEM, with the *P* values (Student's *t* test, two-sided) indicated at the top. Number of TIL-B (**c**) and TIL-T (**d**) cell counts in HLA-A^+ TLSs normalized by the area of the tumor bed (per mm^2). Data are represented as the mean ± SEM, with the *P* values (Student's *t* test, two-sided) indicated at the top. All the panels presented data for responders ($n = 36$) and non-responders ($n = 24$).

HLA-A^+ TLSs are associated with a clinical benefit from ICB treatment for ESCC

The presence of TLSs has been reported to be correlated with patients' positive responses to immunotherapy in various cancers [11–13, 53–55]. After identifying the presence of HLA-A^+ TLSs and demonstrating that the elevated expression of the APM signature represents the reactivation of TLS-resident TIL-Ts, we next investigated whether HLA-A^+ TLSs can be used as an indicator of immunotherapy response in ESCC patients. We quantified HLA-A^+ TLSs on resected ESCC tumor tissues from cohort 2 (36 responders vs. 24 non-responders) and found that the normalized number and area of HLA-A^+ TLSs in the tumor bed were significantly or marginally significantly increased in the responders ($P = 0.026$ and 0.062, respectively) (Fig. 5a, b). In contrast, no significant difference was observed for either the normalized number or area of HLA-A^- TLSs (Supplementary Fig. S13a, b).

We also quantified TIL-Bs in HLA-A$^+$ TLSs in the tumor bed and found that the number of TIL-Bs inside HLA-A$^+$ TLSs is significantly higher in the responder group ($P = 0.032$) (Fig. 5c). However, no significant difference was observed in the number of TIL-Bs in HLA-A$^-$ TLSs ($P = 0.66$) (Supplementary Fig. S13c). Similar results were observed for TLS-resident TIL-Ts (Fig. 5d and Supplementary Fig. S13d). Overall, these findings suggest that HLA-A$^+$ TLSs and its major cellular components (TIL-Ts and TIL-Bs) are elevated in responders, further supporting our finding that TLS-resident TIL-Ts that demonstrate elevated expression of the APM signature are reactivated with the antitumor response.

DISCUSSION

Tumor patients greatly benefit from recent advances in innovative ICB therapy for multiple tumors, including ESCC. It is commonly believed that immune checkpoint inhibitors, such as anti-PD-1 antibodies, exert antitumor actions by reactivating exhausted cytotoxic CD8$^+$ T cells. Recent findings also showed that B cell responses within TLSs may exert another immune pressure against tumors after ICB treatment [56, 57]. In the present work, we showed that tumors from ICB-responsive ESCC patients feature elevated expression of an APM signature. Regardless of whether ICB treatment is administered, ESCC tumors contain HLA-A$^+$ TLSs. TLS-resident cells increasingly express HLA-A as TLSs mature. Exhausted CD8$^+$ and CD4$^+$ TIL-Ts in TLSs are reactivated and show elevated expression of the APM signature as TLSs mature. Finally, HLA-A$^+$ TLSs and their major cellular components, TIL-Ts and TIL-Bs, are associated with a clinical benefit from ICB treatment in ESCC patients.

Recent studies have revealed that exhausted CD8$^+$ T cells (Tex) are more heterogenous than previously understood, which include not only stem-like progenitor or terminal differentiated subtypes but also cells in intermediate states, such as a transitory cell population [38, 58], or intermediate Tex (Tex^{int}) [59]. Contrary to terminal differentiated Tex, which have lost the capacity to proliferate, the transitional [38, 58] or Tex^{int} [59] retain the potential to differentiate into effector cells. The intricate relationships between these Tex subtypes and various Tex states identified in our work (Tex_S1 to Tex_S4) warrant further exploration.

Our work showed that TLS-resident cells increasingly express HLA-A as TLSs mature, but the precise initiation time of HLA-A expression remains unclear. It has been shown that, after the aggregation of lymphocytes, the appearance of a network of distinct CD21$^+$ follicular dendritic cells (fDCs) is important for the maturation of SLOs [60]. The presence of fDCs is critical not only in guiding the distribution of lymphocytes through the production of homeostatic chemokines, such as CXCL13 [60], but also in inducing the differentiation of B cells into memory B cells or plasma cells during GC reactions [61, 62]. Thus, it is intriguing to investigate whether TLS-resident fDCs are required for the appearance of HLA-A$^+$ TLSs.

A notable constraint of our work is the reliance on HLA-A expression as an indirect measurement of the APM signature in mIHC staining. Despite the observation of a strong correlation between *HLA-A* expression and the APM signature in our RNA-seq data ($R = 0.93$, $P = 3.2 \times 10^{-11}$, Supplementary Fig. S6a) and data from ESCC patients in the TCGA ($R = 0.92$, $P < 2.2 \times 10^{-16}$, Supplementary Fig. S6b), it may not fully justify using the protein level of HLA-A as a surrogate marker for the protein level of the entire APM signature.

Another limitation of our study is that even though DSP and scRNA-seq results indicate that TLS-resident APM-expressing TIL-Ts may be reactivated, the mechanistic role the antigen presenting machinery in TLSs on patient outcomes remains elusive. Whether TLS-resident HLA-A-expressing cells, mainly TIL-B and TIL-T lymphocytes, can work as antigen-presenting cells (APCs) to display tumor-derived antigens to activate TIL-T lymphocytes in TLSs is worthy of further investigation. An alternative possibility is that the elevated expression of HLA-A simply reflects the reactivated microenvironment of TLSs. This explanation is consistent with the observed strong positive correlation between the gene signatures of APM and IFN-γ (Supplementary Fig. S5), which is a cytokine known to be capable of stimulating *HLA* class I gene expression [63, 64] through the binding of interferon response factors to IFN-stimulated response element binding motifs located within the promoter regions of *HLA* class I genes [65]. This is also in line with the well-established association between IFN-γ and immunotherapy response in multiple cancer types [28], including gastric cancer [66], melanoma [67] and non-small cell lung cancer [68]. The elevated levels of IFN-γ in TLSs may contribute to the increased expression of HLA-A in HLA-A$^+$ TLSs. Regardless of the underlying mechanism, giving that HLA-A is readily detectable as a surface membrane protein, while IFN-γ cannot be easily evaluated as a secreted protein through conventional immunohistochemistry staining, our work has showed that HLA-A$^+$ TLSs are associated with a clinical benefit from ICB treatment for ESCC, and may serve a promising biomarker capable of predicting the clinical benefit of ICB therapy.

DATA AVAILABILITY

The RNA-seq data can be accessed on the Genome Sequence Archive in National Genomics Data Center, China National Center for Bioinformation / Beijing Institute of Genomics repository (https://ngdc.cncb.ac.cn/gsa-human) under the accession number HRA006820. The scRNA-seq data was downloaded from the GEO repository under the accession number GSE160269 [36].

REFERENCES

1. Bray F, Ferlay J, Soerjomataram I, Siegel RL, Torre LA, Jemal A. Global cancer statistics 2018: GLOBOCAN estimates of incidence and mortality worldwide for 36 cancers in 185 countries. CA Cancer J Clin. 2018;68:394–424.
2. Chen W, Zheng R, Baade PD, Zhang S, Zeng H, Bray F, et al. Cancer statistics in China, 2015. CA Cancer J Clin. 2016;66:115–32.
3. Liu J, Xie X, Zhou C, Peng S, Rao D, Fu J. Which factors are associated with actual 5-year survival of oesophageal squamous cell carcinoma? Eur J Cardiothorac Surg. 2012;41:e7–11.
4. Peng Q, Qiu X, Zhang Z, Zhang S, Zhang Y, Liang Y, et al. PD-L1 on dendritic cells attenuates T cell activation and regulates response to immune checkpoint blockade. Nat Commun. 2020;11:4835.
5. Kojima T, Shah MA, Muro K, Francois E, Adenis A, Hsu CH, et al. Randomized Phase III KEYNOTE-181 Study of Pembrolizumab Versus Chemotherapy in Advanced Esophageal Cancer. J Clin Oncol. 2020;38:4138–48.
6. Kato K, Cho BC, Takahashi M, Okada M, Lin CY, Chin K, et al. Nivolumab versus chemotherapy in patients with advanced oesophageal squamous cell carcinoma refractory or intolerant to previous chemotherapy (ATTRACTION-3): a multicentre, randomised, open-label, phase 3 trial. Lancet Oncol. 2019;20:1506–17.
7. Baba Y, Nomoto D, Okadome K, Ishimoto T, Iwatsuki M, Miyamoto Y, et al. Tumor immune microenvironment and immune checkpoint inhibitors in esophageal squamous cell carcinoma. Cancer Sci. 2020;111:3132–41.
8. Sautes-Fridman C, Petitprez F, Calderaro J, Fridman WH. Tertiary lymphoid structures in the era of cancer immunotherapy. Nat Rev Cancer. 2019;19:307–25.
9. Schumacher TN, Thommen DS. Tertiary lymphoid structures in cancer. Science. 2022;375:eabf9419.
10. Chen Z, Wang X, Jin Z, Li B, Jiang D, Wang Y, et al. Deep learning on tertiary lymphoid structures in hematoxylin-eosin predicts cancer prognosis and immunotherapy response. NPJ Precis Oncol. 2024;8:73.
11. Helmink BA, Reddy SM, Gao J, Zhang S, Basar R, Thakur R, et al. B cells and tertiary lymphoid structures promote immunotherapy response. Nature. 2020;577:549–55.
12. Cabrita R, Lauss M, Sanna A, Donia M, Skaarup Larsen M, Mitra S, et al. Tertiary lymphoid structures improve immunotherapy and survival in melanoma. Nature. 2020;577:561–5.
13. Petitprez F, de Reynies A, Keung EZ, Chen TW, Sun CM, Calderaro J, et al. B cells are associated with survival and immunotherapy response in sarcoma. Nature. 2020;577:556–60.
14. Eisenhauer EA, Therasse P, Bogaerts J, Schwartz LH, Sargent D, Ford R, et al. New response evaluation criteria in solid tumours: revised RECIST guideline (version 1.1). Eur J Cancer. 2009;45:228–47.

15. Bray NL, Pimentel H, Melsted P, Pachter L. Near-optimal probabilistic RNA-seq quantification. Nat Biotechnol. 2016;34:525–7.
16. Wu T, Hu E, Xu S, Chen M, Guo P, Dai Z, et al. clusterProfiler 4.0: A universal enrichment tool for interpreting omics data. Innovation. 2021;2:100141.
17. Bolotin DA, Poslavsky S, Mitrophanov I, Shugay M, Mamedov IZ, Putintseva EV, et al. MiXCR: software for comprehensive adaptive immunity profiling. Nat Methods. 2015;12:380–1.
18. de Masson A, O'Malley JT, Elco CP, Garcia SS, Divito SJ, Lowry EL, et al. High-throughput sequencing of the T cell receptor beta gene identifies aggressive early-stage mycosis fungoides. Sci Transl Med. 2018;10:eaar5894.
19. Love MI, Huber W, Anders S. Moderated estimation of fold change and dispersion for RNA-seq data with DESeq2. Genome Biol. 2014;15:550.
20. Hao Y, Hao S, Andersen-Nissen E, Mauck WM 3rd, Zheng S, Butler A, et al. Integrated analysis of multimodal single-cell data. Cell. 2021;184:3573–3587 e3529.
21. McGinnis CS, Murrow LM, Gartner ZJ. DoubletFinder: Doublet Detection in Single-Cell RNA Sequencing Data Using Artificial Nearest Neighbors. Cell Syst. 2019;8:329–37.e324.
22. Korsunsky I, Millard N, Fan J, Slowikowski K, Zhang F, Wei K, et al. Fast, sensitive and accurate integration of single-cell data with Harmony. Nat Methods. 2019;16:1289–96.
23. Aran D, Looney AP, Liu L, Wu E, Fong V, Hsu A, et al. Reference-based analysis of lung single-cell sequencing reveals a transitional profibrotic macrophage. Nat Immunol. 2019;20:163–72.
24. Trapnell C, Cacchiarelli D, Grimsby J, Pokharel P, Li S, Morse M, et al. The dynamics and regulators of cell fate decisions are revealed by pseudotemporal ordering of single cells. Nat Biotechnol. 2014;32:381–6.
25. Newman AM, Liu CL, Green MR, Gentles AJ, Feng W, Xu Y, et al. Robust enumeration of cell subsets from tissue expression profiles. Nat Methods. 2015;12:453–7.
26. Chen B, Khodadoust MS, Liu CL, Newman AM, Alizadeh AA. Profiling Tumor Infiltrating Immune Cells with CIBERSORT. Methods Mol Biol. 2018;1711:243–59.
27. Sharonov GV, Serebrovskaya EO, Yuzhakova DV, Britanova OV, Chudakov DM. B cells, plasma cells and antibody repertoires in the tumour microenvironment. Nat Rev Immunol. 2020;20:294–307.
28. Ayers M, Lunceford J, Nebozhyn M, Murphy E, Loboda A, Kaufman DR, et al. IFN-gamma-related mRNA profile predicts clinical response to PD-1 blockade. J Clin Invest. 2017;127:2930–40.
29. Senbabaoglu Y, Gejman RS, Winer AG, Liu M, Van Allen EM, de Velasco G, et al. Tumor immune microenvironment characterization in clear cell renal cell carcinoma identifies prognostic and immunotherapeutically relevant messenger RNA signatures. Genome Biol. 2016;17:231.
30. Jiang Y, Li Y, Zhu B. T-cell exhaustion in the tumor microenvironment. Cell Death Dis. 2015;6:e1792.
31. Gu-Trantien C, Loi S, Garaud S, Equeter C, Libin M, de Wind A, et al. CD4(+) follicular helper T cell infiltration predicts breast cancer survival. J Clin Invest. 2013;123:2873–92.
32. Zhang Y, Chen H, Mo H, Hu X, Gao R, Zhao Y, et al. Single-cell analyses reveal key immune cell subsets associated with response to PD-L1 blockade in triple-negative breast cancer. Cancer Cell. 2021;39:1578–93.e1578.
33. Thommen DS, Koelzer VH, Herzig P, Roller A, Trefny M, Dimeloe S, et al. A transcriptionally and functionally distinct PD-1(+) CD8(+) T cell pool with predictive potential in non-small-cell lung cancer treated with PD-1 blockade. Nat Med. 2018;24:994–1004.
34. Liu B, Hu X, Feng K, Gao R, Xue Z, Zhang S, et al. Temporal single-cell tracing reveals clonal revival and expansion of precursor exhausted T cells during anti-PD-1 therapy in lung cancer. Nat Cancer. 2022;3:108–21.
35. Groeneveld CS, Fontugne J, Cabel L, Bernard-Pierrot I, Radvanyi F, Allory Y, et al. Tertiary lymphoid structures marker CXCL13 is associated with better survival for patients with advanced-stage bladder cancer treated with immunotherapy. Eur J Cancer. 2021;148:181–9.
36. Zhang X, Peng L, Luo Y, Zhang S, Pu Y, Chen Y, et al. Dissecting esophageal squamous-cell carcinoma ecosystem by single-cell transcriptomic analysis. Nat Commun. 2021;12:5291.
37. Jansen CS, Prokhnevska N, Master VA, Sanda MG, Carlisle JW, Bilen MA, et al. An intra-tumoral niche maintains and differentiates stem-like CD8 T cells. Nature. 2019;576:465–70.
38. Eberhardt CS, Kissick HT, Patel MR, Cardenas MA, Prokhnevska N, Obeng RC, et al. Functional HPV-specific PD-1(+) stem-like CD8 T cells in head and neck cancer. Nature. 2021;597:279–84.
39. Horton BL, Morgan DM, Momin N, Zagorulya M, Torres-Mejia E, Bhandarkar V, et al. Lack of CD8(+) T cell effector differentiation during priming mediates checkpoint blockade resistance in non-small cell lung cancer. Sci Immunol. 2021;6:eabi8800.
40. Philip M, Schietinger A. CD8(+) T cell differentiation and dysfunction in cancer. Nat Rev Immunol. 2022;22:209–23.
41. Sade-Feldman M, Yizhak K, Bjorgaard SL, Ray JP, de Boer CG, Jenkins RW, et al. Defining T Cell States Associated with Response to Checkpoint Immunotherapy in Melanoma. Cell. 2018;175:998–1013.e1020.
42. Miller BC, Sen DR, Al Abosy R, Bi K, Virkud YV, LaFleur MW, et al. Subsets of exhausted CD8(+) T cells differentially mediate tumor control and respond to checkpoint blockade. Nat Immunol. 2019;20:326–36.
43. Brummelman J, Mazza EMC, Alvisi G, Colombo FS, Grilli A, Mikulak J, et al. High-dimensional single cell analysis identifies stem-like cytotoxic CD8(+) T cells infiltrating human tumors. J Exp Med. 2018;215:2520–35.
44. Kurtulus S, Madi A, Escobar G, Klapholz M, Nyman J, Christian E, et al. Checkpoint Blockade Immunotherapy Induces Dynamic Changes in PD-1(-)CD8(+) Tumor-Infiltrating T Cells. Immunity. 2019;50:181–94.e186.
45. Prokhnevska N, Cardenas MA, Valanparambil RM, Sobierajska E, Barwick BG, Jansen C, et al. CD8(+) T cell activation in cancer comprises an initial activation phase in lymph nodes followed by effector differentiation within the tumor. Immunity. 2023;56:107–24.e105.
46. Kwon BS, Weissman SM. cDNA sequences of two inducible T-cell genes. Proc Natl Acad Sci USA. 1989;86:1963–7.
47. Melero I, Bach N, Hellstrom KE, Aruffo A, Mittler RS, Chen L. Amplification of tumor immunity by gene transfer of the co-stimulatory 4-1BB ligand: synergy with the CD28 co-stimulatory pathway. Eur J Immunol. 1998;28:1116–21.
48. Salgado FJ, Lojo J, Fernandez-Alonso CM, Vinuela J, Cordero OJ, Nogueira M. Interleukin-dependent modulation of HLA-DR expression on CD4and CD8 activated T cells. Immunol Cell Biol. 2002;80:138–47.
49. Alspach E, Lussier DM, Schreiber RD. Interferon gamma and Its Important Roles in Promoting and Inhibiting Spontaneous and Therapeutic Cancer Immunity. Cold Spring Harb Perspect Biol. 2019;11:a028480.
50. Buchan SL, Dou L, Remer M, Booth SG, Dunn SN, Lai C, et al. Antibodies to Costimulatory Receptor 4-1BB Enhance Anti-tumor Immunity via T Regulatory Cell Depletion and Promotion of CD8 T Cell Effector Function. Immunity. 2018;49:958–70.e957.
51. Shaikh RB, Santee S, Granger SW, Butrovich K, Cheung T, Kronenberg M, et al. Constitutive expression of LIGHT on T cells leads to lymphocyte activation, inflammation, and tissue destruction. J Immunol. 2001;167:6330–7.
52. Chen L, Flies DB. Molecular mechanisms of T cell co-stimulation and co-inhibition. Nat Rev Immunol. 2013;13:227–42.
53. van Dijk N, Gil-Jimenez A, Silina K, Hendricksen K, Smit LA, de Feijter JM, et al. Preoperative ipilimumab plus nivolumab in locoregionally advanced urothelial cancer: the NABUCCO trial. Nat Med. 2020;26:1839–44.
54. Gao J, Navai N, Alhalabi O, Siefker-Radtke A, Campbell MT, Tidwell RS, et al. Neoadjuvant PD-L1 plus CTLA-4 blockade in patients with cisplatin-ineligible operable high-risk urothelial carcinoma. Nat Med. 2020;26:1845–51.
55. Liu Z, Meng X, Tang X, Zou W, He Y. Intratumoral tertiary lymphoid structures promote patient survival and immunotherapy response in head neck squamous cell carcinoma. Cancer Immunol Immunother. 2023;72:1505–21.
56. Barros LRC, Souza-Santos PT, Pretti MAM, Vieira GF, Bragatte MAS, Mendes MFA, et al. High infiltration of B cells in tertiary lymphoid structures, TCR oligoclonality, and neoantigens are part of esophageal squamous cell carcinoma microenvironment. J Leukoc Biol. 2020;108:1307–18.
57. Meylan M, Petitprez F, Becht E, Bougouin A, Pupier G, Calvez A, et al. Tertiary lymphoid structures generate and propagate anti-tumor antibody-producing plasma cells in renal cell cancer. Immunity. 2022;55:527–41.e525.
58. Hudson WH, Gensheimer J, Hashimoto M, Wieland A, Valanparambil RM, Li P, et al. Proliferating Transitory T Cells with an Effector-like Transcriptional Signature Emerge from PD-1(+) Stem-like CD8(+) T Cells during Chronic Infection. Immunity. 2019;51:1043–58.e1044.
59. Beltra JC, Manne S, Abdel-Hakeem MS, Kurachi M, Giles JR, Chen Z, et al. Developmental Relationships of Four Exhausted CD8(+) T Cell Subsets Reveals Underlying Transcriptional and Epigenetic Landscape Control Mechanisms. Immunity. 2020;52:825–41.e828.
60. Mebius RE. Organogenesis of lymphoid tissues. Nat Rev Immunol. 2003;3:292–303.
61. Bergomas F, Grizzi F, Doni A, Pesce S, Laghi L, Allavena P, et al. Tertiary intratumor lymphoid tissue in colo-rectal cancer. Cancers. 2011;4:1–10.
62. Di Caro G, Bergomas F, Grizzi F, Doni A, Bianchi P, Malesci A, et al. Occurrence of tertiary lymphoid tissue is associated with T-cell infiltration and predicts better prognosis in early-stage colorectal cancers. Clin Cancer Res. 2014;20:2147–58.
63. Zhou F. Molecular mechanisms of IFN-gamma to up-regulate MHC class I antigen processing and presentation. Int Rev Immunol. 2009;28:239–60.
64. Zhang S, Kohli K, Black RG, Yao L, Spadinger SM, He Q, et al. Systemic Interferon-gamma Increases MHC Class I Expression and T-cell Infiltration in Cold Tumors: Results of a Phase 0 Clinical Trial. Cancer Immunol Res. 2019;7:1237–43.
65. Sznarkowska A, Mikac S, Pilch M. MHC Class I Regulation: The Origin Perspective. Cancers. 2020;12:1155.

66. Li S, Li K, Tian F, Li H, Xia Q, Li T, et al. A high interferon gamma signature of CD8(+) T cells predicts response to neoadjuvant immunotherapy plus chemotherapy in gastric cancer. Front Immunol. 2022;13:1056144.
67. Grasso CS, Tsoi J, Onyshchenko M, Abril-Rodriguez G, Ross-Macdonald P, Wind-Rotolo M, et al. Conserved Interferon-gamma Signaling Drives Clinical Response to Immune Checkpoint Blockade Therapy in Melanoma. Cancer Cell. 2020;38:500–15.e503.
68. Karachaliou N, Crespo G, Aldeguer E, Drozdowskyj A, Gimenez Capitan A, Teixido C, et al. Interferon-gamma (INFG), an important marker of response to immune checkpoint blockade (ICB) in non-small cell lung cancer (NSCLC) and melanoma patients. J Clin Oncol. 2017;35:11504.

ACKNOWLEDGEMENTS

We thank Shaoyang Sun at Fudan University for the assistance with the experiment.

FUNDING

This work was supported by funding from the National Key R&D Program of China (2021YFC2501004), the National Natural Science Foundation of China (82171837, 82188102, 82030089, 82225033), the CAMS Innovation Fund for Medical Sciences (2021-I2M-1-067), the Fundamental Research Funds for the Central Universities (3332021091), Non-profit central research institute fund of Chinese Academy of Medical Sciences (2022-RC310-08), the Science and Technology Commission of Shanghai Municipality (23JS1400400), Shanghai Municipal Science and Technology Major Project (2017SHZDZX01 and 2018SHZDZX01) and ZJLab.

AUTHOR CONTRIBUTIONS

ZL, YL and YJ conceived and supervised the study. DZ performed experiments. DZ, JM and XX analyzed and interpreted the data, with assistance from ZC, MJ, WY, JW, WM and WQ. DJ, LJ and XW recruited patients under the supervision of YH and JH. DJ and LJ gathered clinical data. DZ, JM and YL wrote the manuscript with assistance from all authors. All authors read and approved the final manuscript.

COMPETING INTERESTS

The authors declare no competing interests.

ETHICS APPROVAL AND CONSENT TO PARTICIPATE

Written informed consent was obtained from each participant. The study was conducted following the principles outlined in the Declaration of Helsinki and was approved by the Ethics Committees of Cancer Hospital, Chinese Academy of Medical Science, Beijing, China (Approval No. 16-008/1087), and Zhongshan Hospital, Fudan University, Shanghai, China (Approval No. B2022-632).

ADDITIONAL INFORMATION

Supplementary information The online version contains supplementary material available at https://doi.org/10.1038/s41416-024-02712-9.

Correspondence and requests for materials should be addressed to Yuchen Jiao, Yun Liu or Zhihua Liu.